PCCP

PAPER

View Article Online
View Journal | View Issue

Cite this: *Phys. Chem. Chem. Phys.*, 2016, **18**, 21442

Quantum effects in ultrafast electron transfers within cryptochromes†

Thiago Firmino,‡[a] Etienne Mangaud,‡[ab] Fabien Cailliez,[a] Adrien Devolder,[ac] David Mendive-Tapia,[d] Fabien Gatti,[d] Christoph Meier,*[b] Michèle Desouter-Lecomte*[ae] and Aurélien de la Lande*[a]

Cryptochromes and photolyases are flavoproteins that may undergo ultrafast charge separation upon electronic excitation of their flavin cofactors. Charge separation involves chains of three or four tryptophan residues depending on the protein of interest. The molecular mechanisms of these processes are not completely clear. In the present work we investigate the relevance of quantum effects like the occurrence of nuclear tunneling and of coherences upon charge transfer in *Arabidopsis thaliana* cryptochromes. The possible breakdown of the Condon approximation is also investigated. We have devised a simulation protocol based on the realization of molecular dynamics simulations on diabatic potential energy surfaces defined at the hybrid constrained density functional theory/molecular mechanics level. The outcomes of the simulations are analyzed through various dedicated kinetics schemes related to the Marcus theory that account for the aforementioned quantum effects. MD simulations also provide a basic material to define realistic model Hamiltonians for subsequent quantum dissipative dynamics. To carry out quantum simulations, we have implemented an algorithm based on the Hierarchical Equations of Motion. With this new tool in hand we have been able to model the electron transfer chain considering either two- or three-state models. Kinetic models and quantum simulations converge to the conclusion that quantum effects have a significant impact on the rate of charge separation. Nuclear tunneling involving atoms of the tryptophan redox cofactors as well as of the environment (protein atoms and water molecules) is significant. On the other hand non-Condon effects are negligible in most simulations. Taken together, the results of the present work provide new insights into the molecular mechanisms controlling charge separation in this family of flavoproteins.

Received 27th April 2016,
Accepted 27th June 2016

DOI: 10.1039/c6cp02809h

www.rsc.org/pccp

1. Introduction

Photoinduced electron transfers (ETs) in photosynthetic reaction centers (PRCs), in cryptochromes (Cry) and in DNA photolyases (Pl), are among the fastest charge transfer processes encountered in proteins.[1,2] ETs in PRCs have been extensively studied since the first time-resolved experiments on these proteins.[3,4] In these proteins the so-called special pair or chlorophyll molecule is able to deliver electrons to a bacteriopheophytin in less than 10 ps after electronic excitation. Forty years of research have permitted the accumulation of a large amount of experimental and computational evidence and this ultrafast ET can now be seen as rather well understood.[5] ETs in Crys and Pls have been less investigated, probably because of their more recent discoveries.[6] Crys and Pls form a superfamily of ubiquitous proteins that share strong structural similarities, despite having very versatile biological functions depending on the organisms in which they are expressed.[2] In particular they all feature a Flavin Adenosine Diphosphate (FAD) cofactor folded in an uncommon U-shape.[7,8] The redox state of the FAD cofactor may either be the fully oxidized state or the hydroquinone (semi-, $1e^-$ reduced form). Upon electronic excitation, either by direct absorption of photons like during *in vitro* experiments or by electronic energy transfer from other pigments, the flavin cofactor may abstract an electron from a nearby tryptophan residue (W_A) to form an $FAD^{\bullet -}$, $W_A^{\bullet +}$ radical pair.[1] If the flavin is initially in its fully oxidized state this primary ET usually

[a] *Laboratoire de Chimie Physique, CNRS, Université Paris-Sud, Université Paris Saclay, Orsay F-91405, France. E-mail: michele.desouter-lecomte@u-psud.fr, aurelien.de-la-lande@u-psud.fr*
[b] *Laboratoire Collisions Agrégats Réactivité, UMR 5589, IRSAMC, Université Toulouse III Paul Sabatier, F-31062, Toulouse, France. E-mail: chris@irsamc.ups-tlse.fr*
[c] *Laboratoire de Chimie Quantique et Photophysique, CP160/09, Université Libre de Bruxelles, B-1050 Brussels, Belgium*
[d] *CTMM, Institut Charles Gerhardt UMR 5253, CNRS/Université de Montpellier, France*
[e] *Département de Chimie, Université de Liège, Sart Tilman, B6, B-4000 Liège, Belgium*

† Electronic supplementary information (ESI) available. See DOI: 10.1039/c6cp02809h

‡ These authors equally contributed to this work.

takes place on the sub-picosecond timescale;[9–12] otherwise, when starting from the FADH• form, the primary reduction to $FADH^-$ takes a longer time (>ps).[13] Beyond residue W_A, a few other tryptophan residues (W_B, W_C, ...) are aligned in all these proteins. They allow rapid hole migration to form a long-range charge-separated state. The chain of W cofactors may be comprised of three or four residues depending on the protein: most of the proteins contain a tryptophan triad but animal cryptochromes and animal (6-4) photolyases contain tryptophan tetrads.[14] Studying charge separation in this family of proteins is motivating for several reasons. First it takes place on the picosecond time scale meaning that several protein vibrational modes certainly don't have time to equilibrate on the time scale of ET. This particularity may be at the source of various non-ergodic effects that may be of interest, for example accelerated charge transport or reduced heat released to the medium.[15] In the PRC, this situation leads for example to interesting conclusions that partially changed our understanding of these processes. In *Escherichia coli* CPD (cyclobutan pyrimidine dimer) Pl as well as in *Xenopus laevis* (6-4) photolyase (hereafter referred to as *Xl* (6-4) Pl), it was recently shown by molecular dynamics simulations that ET proceeds out of thermal equilibrium.[16,17] In this work we are interested in *Arabidopsis thaliana* cryptochromes (*At*Cry). We recently reported a computational study of the influence of ATP binding in the vicinity of FAD on the kinetics of the primary ET step (W_{400} → FAD*, see Fig. 1).[18] The competition with ET from the adenine fragment of the FAD cofactor was also investigated.[18]

In this article we pursue our investigations by examining the subsequent charge separation process within the tryptophan triad. In *At*Cry the (W_A, W_B, W_C) triad is composed of residues 400, 377 and 324 respectively. Other groups reported insightful computational studies of electron transfers in the same protein using more coarse-grained approaches.[20] In the present work we address aspects that were not considered in previous publications, namely the realization of ET beyond the Condon approximation or the involvement of nuclear tunneling in the ET mechanism. To this end we report hybrid constrained density functional theory[21–23]/molecular mechanics (cDFT/MM) molecular dynamics (MD) simulations of the two electronic transfer W_{377} → W_{400}^+ (ET1) and W_{324} → W_{377}^+ (ET2) steps.

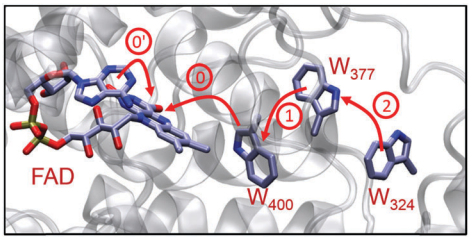

Fig. 1 Zoom on the photoactive site of *At*Cry showing the FAD cofactor and the triad of tryptophan residues involved in charge separation. Electron transfers from W_{400} or the adenine moieties of FAD toward the excited isoalloxazine ring (steps 0 and 0′ respectively) were investigated in ref. 18 Electron transfers in the tryptophan triad are indexed as 1 and 2. Picture prepared by VMD.[19]

This is to our knowledge the first application of such state-of-the-art methodology to a biological ET transfer chain. Dedicated kinetics models for including quantum effects are used to analyze the outputs of MD simulations.[24,25] We further provide a detailed analysis of the respective contributions of protein residues and solvent molecules in ET kinetics.

We finally report the results of Quantum Dissipative Dynamics (QDD) based on the Hierarchical-Equations-of-Motion (HEOM) algorithm, simulating as the whole the charge transfer process within the tryptophan triad. Spectral density functions (J) for each ET steps are extracted from the fluctuations of diabatic energy gaps along cDFT/MM MD trajectories. These data provide basic material for direct QDD[26,27] or Multi-Layers Multi Configuration Time Dependent Hartree (ML-MCTDH) simulations.[28–32] In a previous work we used cDFT to build a reaction path model derived from a spin-boson vibronic Hamiltonian.[33] The methodology was applied at that time to an organic mixed valence molecule under vacuum. In the present work we follow a different approach that allows us to account for the coupling with the outer-sphere degrees of freedom. The spin-boson dynamics is treated exactly by the HEOM method (Hierarchical Equations of Motion) for QDD.[34–43] This approach has already been applied to excitation energy transfer in photosynthetic antenna complexes with insightful results.[44,45] It is applied here to ETs within the tryptophan triad of *At*Cry. This quantum approach completes the classical kinetic description by estimating electronic coherences during the process.

This article is organized as follows. In Section 2 we detail the various theoretical models and the computational procedures followed in this study. Results are presented in Section 3, beginning with the application of the kinetics models to model the two charge transfer steps, and continuing with the results of the quantum dissipative dynamics.

2. Methodology

Marcus theory and the linear response approximation

The Marcus theory (MT) is a powerful formalism for calculating electron transfer rates from a few quantities that are accessible by theoretical calculations or experimental data. Under the Condon approximation and in the perturbative electronic coupling regime, the ET rate can be evaluated by the Fermi Golden Rule[46,47]

$$k_{ET} = \frac{2\pi}{\hbar}|H_{DA}|^2\rho_{FC} \quad (1)$$

where ρ_{FC} is the Franck–Condon (FC) weighted density of states. In the high temperature limit a classical expression is often adopted:[47]

$$\rho_{FC} = \frac{1}{\sqrt{4\pi\lambda k_B T}}\exp\left[-\frac{\Delta A^{\ddagger}}{k_B T}\right] = \frac{1}{\sqrt{4\pi\lambda k_B T}}\exp\left[-\frac{(\Delta A^0+\lambda)^2}{4\lambda k_B T}\right] \quad (2)$$

where $\Delta A^{\ddagger}$ is the activation free energy. ΔA^0 is the reaction free energy, λ is the reorganization energy and H_{DA} is the electronic coupling that couples quantum mechanically the two diabatic

electronic states involved in charge transfer. The reorganization energy is defined as the work needed to drive the system in a given electronic state from its equilibrium position to the equilibrium position of the other electronic state. The other parameters (k_B and T) have their usual meanings. Combining eqn (1) and (2) leads to the well-known Marcus theory non-adiabatic classical rate constant expression:[47]

$$k_{ET}^{MT} = \frac{2\pi}{\hbar}\frac{{H_{DA}}^2}{\sqrt{4\pi\lambda k_B T}}\exp\left[-\frac{\left(\Delta A^0+\lambda\right)^2}{4\lambda k_B T}\right] \quad (3)$$

A key quantity of most ET theories is the vertical energy gap between the diabatic states involved in the charge transfer process.[48] It is defined as $\Delta E = E_f - E_i$ where f and i stand for the final and initial states. The Marcus theory parameters λ and ΔA^0 are accessible from the knowledge of the average energy gaps through the Linear Response Approximation (LRA):[49]

$$\Delta A^0 = \frac{1}{2}\left(\langle\Delta E\rangle_i + \langle\Delta E\rangle_f\right) \quad (4)$$

$$\lambda^{St} = \frac{1}{2}\left(\langle\Delta E\rangle_i - \langle\Delta E\rangle_f\right) \quad (5)$$

$\langle\ldots\rangle_x$ denotes an average performed on a sample of structures extracted from an MD simulation carried out on the potential energy surface corresponding to state x. The St upper-script is there to recall the connection of the reorganization energy with the Stokes shift encountered in optical spectroscopies. The reorganization energy may alternatively be defined from the variance of the energy gap:

$$\lambda_x^{var} = \frac{\langle\delta\Delta E\cdot\delta\Delta E\rangle_x}{2k_B T} \quad (6)$$

where $\delta\Delta E = \Delta E - \langle\Delta E\rangle_x$ is the energy gap fluctuation along MD simulation performed on the electronic state x (i or f). Note that this definition may lead to different values of the reorganization energy for the two electronic states. Actually the LRA is equivalent to the fact that both energy gap distributions in states i and f have Gaussian distributions of similar widths, which leads to:

$$\lambda = \lambda^{St} = \lambda_i^{var} = \lambda_f^{var} \quad (7)$$

The validity of the LRA for biological ETs that take place in the pico-second time domain has been explored by Matyushov and coworkers.[50–52] They studied the primary electron transfer steps in the PRC and observed noticeable deviations from the LRA due to non-ergodicity and/or to high polarizability of the redox cofactors. In such cases, λ^{St} and λ^{var} are not equal anymore and must be distinguished for the calculation of ET rates.[15]

Another way to calculate the reorganization energy is through the integration of the spectral density $J(\omega)$ related to the auto-correlation function of the diabatic energy gap.

$$\lambda^J = \frac{1}{\pi}\int_0^\infty \frac{J(\omega)}{\omega}d\omega \quad (8)$$

$$J(\omega) = \frac{\beta\omega}{2}\int_{-\infty}^{+\infty}\langle\delta\Delta E(0)\delta\Delta E(t)\rangle\exp i\omega t\,dt \quad (9)$$

Actually it can be shown that λ^J and λ^{var} are mathematically equivalent. In practice though, because of cDFT/MM MD simulations are finite in time, small differences between λ^J and λ^{var} are frequent.

Kinetic models operating beyond the standard Marcus non-adiabatic equation

In this work we assess the validity of some of the approximations underlying eqn (3). The first one concerns non-Condon effects that arise when H_{DA} fluctuates very rapidly compared to the fluctuations of the energy gap. H_{DA} fluctuations may be caused by nuclear motions that simultaneously affect the energy gap (ΔE), but also by vibrational modes that are not coupled to the redox process.[53] In such a case the factorization of H_{DA} outside of the Franck–Condon density of state is no longer valid and alternative formulations have to be considered. To model non-Condon effects we have considered the formalism introduced by Troisi *et al.*[24] The formalism is based on a Taylor expansion of the FC factor averaged over mode vibrations. Stopping at the second order, the rate constant reads

$$k_{ET} = k^{(0)} + k^{(2)} \quad (10)$$

$$k^{(0)} = \frac{2\pi}{\hbar}\langle{H_{DA}}^2\rangle\frac{1}{\sqrt{4\pi\lambda^{var}k_B T}}\exp\left(\frac{-\left(\Delta A^0+\lambda^{St}\right)^2}{4\lambda^{var}k_B T}\right) \quad (11)$$

$$k^{(2)} = k^{(0)}\times 2\frac{\hbar^2}{{\tau_{coh}}^2}\left[\frac{\left(\Delta A^0+\lambda^{St}\right)^2 - 2\lambda^{var}k_B T}{\left(4\lambda^{var}k_B T\right)^2}\right](1-R_{coh}) \quad (12)$$

$k^{(0)}$ is similar to eqn (3) except that an average value of the square electronic coupling is used. $k^{(2)}$ is the correction to the rate due to non-Condon effects. Note that the formalism introduced by Troisi *et al.* only accounts for non-Condon effects due to vibrational modes affecting H_{DA} but that don't enter into the FC factor (*i.e.* that don't affect ΔE). R_{coh} is the coherence parameter defined as the ratio $\langle H_{DA}\rangle^2/\langle{H_{DA}}^2\rangle$.[54] τ_{coh} is the coherence time that characterizes how fast the system loses memory of previous electronic coupling values. It is calculated in this work as the time taken for the normalized autocorrelation function of H_{DA} to drop to 1/e (assuming a mono-exponential decay).[55] Note also that in eqn (11) and (12), we make use of the two reorganization energies λ^{St} and λ^{var} (or λ^J), as proposed by Matyushov[15] to take into account the non-ergodicity effects, instead of the unique λ of the "classical" Marcus theory. λ^{var} appears in the prefactor and in the denominator of the exponential because it contributes to define the Gaussian shape of the free energy function by virtue of eqn (6). λ^{St} appears in the numerator of the exponential because it determines the horizontal separation of the bottom of the free energy functions. Again, if the LRA applies $\lambda^{St} = \lambda^{var}$ and the above separation is only formal.[15]

Another type of effect investigated in this work is nuclear tunneling. Indeed the high temperature limit given by eqn (2) is not adapted to account for the coupling of high frequency modes that should be treated at the quantum mechanical level. At 300 K the thermal energy amounts to 200 cm^{-1}. Therefore not only

the intramolecular modes of the tryptophan residues should be treated quantum mechanically, but also probably a large ensemble of environmental degrees of freedom. There have been numerous computational schemes proposed to take this into account. One may for instance employ a Jortner–Bixon formalism,[56,57] as recently illustrated in the case of charge separation within *Xl* (6-4) Pl.[17] Another appealing strategy is to employ the dispersed polaron or spin-boson models.[48,58] In the present work we employ the mixed quantum-classical variant of the Marcus ET rate derived by Stuchebrukhov *et al.*[25] which is based on the spin boson model and assumes the Condon approximation.

$$k = \frac{2\pi}{\hbar}\langle {H_{\mathrm{DA}}}^2\rangle \frac{1}{\sqrt{4\pi\lambda^J(\omega_{\mathrm{qc}})k_{\mathrm{B}}T}} \times \exp\left(\frac{-(\Delta A^0+\lambda^{\mathrm{St}})^2}{4\lambda^J(\omega_{\mathrm{qc}})k_{\mathrm{B}}T} - \frac{1}{\pi\hbar}\int_{\omega_{\mathrm{qc}}}^{\infty}\frac{J(\omega)}{\omega^2}\mathrm{d}\omega\right) \quad (13)$$

The model introduces a cutting frequency (ω_{qc}) to discriminate between classical and quantum modes. Reorganization of the classical degrees of freedom is characterized by $\lambda^J(\omega_{\mathrm{qc}})$ which is calculated using eqn (8) except that the integration is restricted to the $[0,\omega_{\mathrm{qc}}]$ frequency range. Eqn (13) only captures the transition between the ground vibronic states, which could be a limitation. However since the ET steps we are interested in take place in the normal region of the Marcus theory (see Results section), the transition between ground vibronic states are expected to be dominant over vibrationally non-adiabatic reactive channels for which the Franck–Condon terms are weaker. In our recent work on analogous *Xl* (6-4) Pl, we showed that vibrationally non-adiabatic channels actually represented less than 30% of the full rate.[59]

Finally to go beyond the approximation of the kinetic models in order to account for more subtle quantum effects like the occurrence of electronic coherences, we have conducted Dissipative Quantum Dynamics. Details on this type of simulations are given in a subsequent section.

MD simulations on diabatic charge transfer states

To evaluate the quantities described above a computational protocol is necessary to propagate the equations-of-motion of the nuclei and to estimate ΔE. The methodology should also permits to monitor the fluctuations of H_{DA} in the course of the simulations. We wish to employ in this study the most accurate, yet computationally affordable, methodology that will permit us to address the questions listed in Introduction. We chose the constrained DFT approach that we have implemented in deMon2k.[60–62] When coupled to hybrid QM/MM schemes[63] it becomes possible to simulate the dynamics of the protein on the different diabatic states, to evaluate ΔE and H_{DA} on-the-fly with a femtosecond time resolution (or less if needed).[62] Our scheme takes into account polarization of the redox cofactors by the environment. On the other hand we have not yet introduced explicit polarization of the MM parts, a limitation that should be overcome in the future. An advantage of using an additive force field though is that, as described below, ΔE may be decomposed into contributions arising from the different parts of the molecular system (amino-acids, water molecules, counter-ions...), providing insights into the parameters controlling the ET mechanism.

QM/MM approach

The cDFT/MM potential energy function reads:

$$E_{\mathrm{x}} = E^{\mathrm{S+W_2}}_{\mathrm{MM,x}} - E^{\mathrm{W_2}}_{\mathrm{MM,x}} - E^{\mathrm{S/W_2}}_{\mathrm{MM,x}} + E^{\mathrm{W_2pol}}_{\mathrm{DFT,x}} \quad (14)$$

where $E^{\mathrm{S+W_2}}_{\mathrm{MM,x}}$ and $E^{\mathrm{W_2}}_{\mathrm{MM,x}}$ stand for the energy of the full system and of the tryptophan pair (W_2) at the MM level in redox state x. We use the CHARMM C27 force field to calculate these energies.[64–66] The MM force field to describe the Flavin radical $FAD^{\bullet-}$ is described in a previous study.[18] $E^{\mathrm{S/W_2}}_{\mathrm{MM,x}}$ is the classical Coulomb interaction energy between the W_2 pair and the environment atoms and $E^{\mathrm{W_2pol}}_{\mathrm{DFT,x}}$ is the energy of the W_2 pair in the diabatic state x calculated at the cDFT level, with electrostatic embedding composed of the partial charges of the MM environment. The electron density of the redox pair is thus polarized by the point charges of the environment for each redox state. We used the PBE (Perdew, Burke, Ernzerhof)[67] functional combined with the DZVP-GGA (Double Zeta with Valence Polarization functions, calibrated for Generalized Gradient Approximation functionals) basis set.[68] Auxiliary electron densities have been used to calculate the Coulomb and exchange–correlation potentials and energy based on a variational density fitting technique.[69,70] We chose the automatically-generated A2 basis set to expand the auxiliary densities.[71] The two diabatic states were obtained by imposing a net charge difference of ±1 between the two indole rings.[72] The Hirshfeld scheme was used to define the type of atomic charges to be constrained.[73] Tolerance criteria for the energy, charge density coefficients and charge constraints were set to 10^{-7} Ha, 10^{-5} Ha and 10^{-5} e^- respectively. In *ab initio* MD simulations it is uneasy to prevent electronic state switches to take place from one MD step to another. To minimize this risk, we used at every MD step the Molecular Orbitals from the previous step as a guess for the SCF procedure. In addition we applied a projection scheme to ensure that the manifold of occupied MOs remained consistent along the trajectory. The QM and MM outputs were combined to build the QM/MM energy function with the Cuby framework.[74] Cuby implements geometry optimizers and molecular dynamics simulation engines that are compatible with QM/MM schemes.[75] Forces acting on the nuclei were obtained by differentiation of the QM/MM energy given by eqn (14) with respect to coordinates of QM nuclei and MM atoms.[76]

Simulation details

Initial geometries were obtained from our previous study of *At*Cry.[18] The protein was immersed in a 105 Å-edged cubic water box. The system encompasses a total of 110 000 atoms, including around 34 000 of TIP3P[77] water molecules. We refer the reader to ref. 18 for a detailed description of the procedure

to prepare and equilibrate the system. In the present case five structures were extracted from previous classical MD simulations[18] and were further optimized at the MM and QM/MM level to furnish the starting geometries for QM/MM MD simulations. In the following CT1, CT2 and CT3 stand for the diabatic states $\{W^{+}_{400}, W_{377}, W_{324}\}$, $\{W_{400}, W^{+}_{377}, W_{324}\}$ and $\{W_{400}, W_{377}, W^{+}_{324}\}$ respectively. For the first ET step ($W_{377} \rightarrow W_{400}^{+}$, see Fig. 1) five MD simulations were performed on states CT1, monitoring the CT1/CT2 energy gap (ΔE^{1-2}) and electronic coupling every femtosecond. After a few picoseconds of simulations on CT1 we selected a structure for which ΔE^{1-2} was close to zero and we performed MD simulations on CT2 but monitored the CT2/CT3 energy gap (ΔE^{2-3}) and electronic coupling. Similarly, we selected geometries along the CT2 trajectories for which the ΔE^{2-3} gap was close to zero and performed MD simulations on CT3. The lengths of all MD simulations are given Table S1 (ESI†), the sum of which amounts to almost 600 ps. We conducted simulations within the *NVT* ensemble (T = 300 K) using a Nosé–Hoover thermostat with a coupling constant of 0.3 ps^{-1}.[78,79] The integration time step was set to 1 fs. We verified that this time step was small enough for a full temporal resolution of the energy gap fluctuations. Because we do not use periodic boundary conditions in QM/MM MD simulations a layer of water molecules was kept frozen at the borders of the simulation box.

In the present work the molecular fragments that undergo oxidation and reduction (the inner-sphere) are treated at the DFT level. Therefore the MM parameters for the outer-sphere are identical for the different redox states. Thus, given the cDFT/MM energy expression, eqn (14), the energy gap for a generic ET step from the initial (i) to final (f) states, ΔE reduces to

$$\Delta E = E^{W_2 pol}_{DFT,f} - E^{W_2 pol}_{DFT,i} = \Delta E_{inner} + \Delta E_{embed} \quad (15)$$

The decomposition on the r.h.s. of eqn (15) comes from the definition of the DFT energy as a sum over different energy terms, associated with distinct quantum mechanical operators. The first one will be thereafter referred to as the inner-sphere contribution (ΔE_{inner}). It comprises the difference in electron kinetic energy, electron-nuclei Coulomb energy, inter-electron Coulomb repulsion energy and exchange–correlation energy between states i and f. The second contribution refers to the outer-sphere. ΔE_{embed} accounts for the difference in Coulomb attraction between the embedding charges and the tryptophan pair. To analyze more in depth the ET process as a function of the system constituents we found useful to further decompose ΔE_{embed} as $\sum_{k=1}^{N} \Delta E^{k}_{embed}$ where N depends on the level of analysis. For example we could separate the protein contributions from the water contribution. A finer level of analysis would be to look at the contributions of protein residues individually or those of water molecules as a function of distance. The individual components can in principle be extracted from embedding energy calculated at the DFT level. However we found more convenient from a technical point of view to estimate them from a classical Coulomb law. To this end Hirshfeld atomic charges on the W_2 pair atoms were calculated at every MD time step for each diabatic state and the energy gap contribution from a group of atoms, say K, was obtained as

$$\Delta E'^{k}_{embed} = \sum_{A \in W_2} \sum_{i \in K} \frac{(q^{A}_{2} - q^{A}_{1}) q^{i}}{r_{iA}} \quad (16)$$

where r_{iA} is the distance between atoms A and i, q^{A}_{x} and q^{i} are the atomic charges on atom A in state x and of atom i respectively. A prime is used in eqn (16) to emphasize that the embedding energy gap calculated from classical charges is an approximation of the true gap obtained from the QM/MM energy (eqn (15)). However we verified on a test set of a few geometries that the sum of energy gaps $\Delta E'^{k}_{embed}$ thus defined correlates well with the total embedding DFT/MM energy gap (ΔE_{embed}). When the energy gap is decomposed in more than one contribution, the reorganization energy computed from the variance of the energy gap, eqn (6), gives

$$\lambda'^{var}_{embed} = \sum_{k=1}^{n} \lambda'^{var}_{k} + \lambda'_{cross} = \sum_{k=1}^{n} \lambda'^{var}_{k} + \sum_{k=1}^{n} \sum_{l=k+1}^{n} \lambda'^{var}_{k,l} \quad (17)$$

where $\lambda'^{var}_{k} = \langle \delta\Delta E'^{k}_{embed} \cdot \delta\Delta E'^{k}_{embed} \rangle / 2k_B T$ is the reorganization energy contribution of k and $\lambda'^{var}_{k,l} = \langle \delta\Delta E'^{k}_{embed} \cdot \delta\Delta E'^{l}_{embed} \rangle / 2k_B T$ are the cross-terms measuring correlation between contributions. Again primes are used to emphasize that the reorganization energy of the environment obtained from classical charges is an approximation of the one computed from cDFT/MM energies, *i.e.* λ'^{var}_{embed} is an approximation of λ^{var}_{embed} calculated by $\langle \delta\Delta E_{embed} \cdot \delta\Delta E_{embed} \rangle / 2k_B T$.

Electronic coupling calculations

At every MD step two cDFT calculations are carried out, one for each diabatic state of interest. The electronic coupling H_{DA} are then calculated based on the Kohn–Sham determinants of each diabatic states. Because the determinants are not orthogonal, we have followed the projection procedure described in ref. 80 to orthogonalize them. A phase convention was applied to the cDFT wave functions to control the signs of MOs along the trajectories, hence the sign of H_{DA}. Phase convention is mandatory in order to follow the time evolution of signed H_{DA} by its autocorrelation function. At a given MD step, the control procedure was based on the overlap of the MOs with the MOs of the first cDFT calculation of each trajectory that served as reference. H_{DA} was calculated along MD simulations using the PBE functional. It is now established that cDFT coupled with GGA functionals tends to overestimate electronic coupling values due to self-interaction errors.[81,82] This trend was verified on a series of test calculations on a few tens of geometries extracted from the simulations using different exchange–correlation (XC) functionals (see ESI†). Considering hybrid XC functionals with *ca.* 50% of Fock's exchange as references, we derived a scaling factor linking H_{DA} values calculated using PBE0(50%) to those calculated using PBE. H_{DA} calculated along MD trajectories were then scaled down by this correction factor. Fock's exchange contributions to the Kohn–Sham potential were calculated by the recently proposed scheme of Mejia-Rodriguez *et al.*[83]

Model Hamiltonians for DQD

In a first approach, each ET step ET^j with $j = 1, 2$ can be described by a generic spin-boson Hamiltonian[84] written here in mass weighted coordinates:

$$H_j = \begin{pmatrix} 0 & H_{\mathrm{DA},j} \\ H_{\mathrm{DA},j} & \Delta_j \end{pmatrix} + \begin{pmatrix} \frac{1}{2}\sum_i \left(p_i^2 + \omega_i^2 q_i^2\right) & 0 \\ 0 & \frac{1}{2}\sum_i \left(p_i^2 + \omega_i^2 (q_i - d_{i,j})^2\right) \end{pmatrix} \quad (18)$$

where Δ_j is the energy gap and the q_i are the normal modes which are assumed to be the same in both states. Each mode has the same frequency but has a different equilibrium geometry. By choosing the reference point at the minimum of the first state, the vibrational modes are displaced by $d_{i,j}$ in the second state. This Hamiltonian can be partitioned into an electronic effective system Hamiltonian $H_{\mathrm{s},j}$ containing a renormalization (or reorganization) energy λ_j, a vibrational bath $H_{\mathrm{B},j}$ formed by the intramolecular and of the environment (protein, solvent) modes and a system–bath coupling $H_{\mathrm{SB},j}$:

$$H_j = H_{\mathrm{s},j} + H_{\mathrm{B},j} + H_{\mathrm{SB},j} \quad (19a)$$

$$= \begin{pmatrix} 0 & H_{\mathrm{DA},j} \\ H_{\mathrm{DA},j} & \Delta_j + \lambda_j \end{pmatrix} + \frac{1}{2}\sum_i \left(p_i^2 + \omega_i^2 q_i^2\right)\begin{pmatrix} 1 & 0 \\ 0 & 1 \end{pmatrix} + \sum_i \omega_i^2 d_{i,j} q_i \begin{pmatrix} 0 & 0 \\ 0 & -1 \end{pmatrix} \quad (19b)$$

$$= H_{\mathrm{s},j} + H_{\mathrm{B},j} + S_j B_j \quad (19c)$$

where $\lambda_j = 1/2\sum_i \omega_i^2 d_{i,j}^2$. The electronic bias Δ_j is estimated using eqn (4) and the electronic coupling is taken to be the quadratic average $H_{\mathrm{DA}} = \sqrt{\langle H_{\mathrm{DA}}^2(t)\rangle}$ of time series of the electronic coupling generated by the cDFT/MM MD simulations. The reorganization energy is related to the spectral density as shown below. The system–bath coupling involves a collective coordinate of the bath $B_j = \sum_i \omega_i^2 d_{i,j} q_i = \sum_i c_{i,j} q_i$ and a two by two system matrix S_j. This coupling induces a variation of the energy gap linear in the nuclear displacements. For numerical convenience, the origin of the oscillator is usually taken at the middle of both equilibrium geometries. Then the new normal coordinates become $q_i = \bar{q}_i + d_{i,j}/2$ and the Hamiltonian reads

$$H_j = \begin{pmatrix} \lambda_j/4 & H_{\mathrm{DA},j} \\ H_{\mathrm{DA},j} & \Delta_j + \lambda_j/4 \end{pmatrix} + \frac{1}{2}\sum_i \left(p_i^2 + \omega_i^2 \bar{q}_i^2\right)\begin{pmatrix} 1 & 0 \\ 0 & 1 \end{pmatrix} + \sum_i \omega_i^2 d_{i,j}\bar{q}_i \begin{pmatrix} 1/2 & 0 \\ 0 & -1/2 \end{pmatrix} \quad (20)$$

In the three-state case, we set $|1\rangle = |W_{400}{}^{+}W_{377}W_{324}\rangle$, $|2\rangle = |W_{400}W_{377}{}^{+}W_{324}\rangle$ and $|3\rangle = |W_{400}W_{377}W_{324}{}^{+}\rangle$. We assume that each state interacts only with the neighboring ones and that there are two uncorrelated vibrational baths, one for ET1 and one for ET2. The corresponding Hamiltonian takes the following form by setting the origin of the energy scale in the $|2\rangle = |W_{400}W_{377}{}^{+}W_{324}\rangle$ state:

$$H^{(3)} = \begin{pmatrix} -\Delta_1 & H_{\mathrm{DA},1} & 0 \\ H_{\mathrm{DA},1} & 0 & H_{\mathrm{DA},2} \\ 0 & H_{\mathrm{DA},2} & \Delta_2 \end{pmatrix} + \begin{pmatrix} \frac{1}{2}\sum_i \left(p_i^2 + \omega_i^2 (q_i - d_{i,1})^2\right) & 0 & 0 \\ 0 & \frac{1}{2}\sum_i \left(p_i^2 + \omega_i^2 q_i^2\right) & 0 \\ 0 & 0 & \frac{1}{2}\sum_i \left(p_i^2 + \omega_i^2 (q_i - d_{i,2})^2\right) \end{pmatrix} \quad (21)$$

This tight-binding model assumes no direct electronic coupling between states $|1\rangle$ and $|3\rangle$ which is reasonable given the larger distance separating W_{400} and W_{324} than between W_{400} and W_{377} or W_{377} and W_{324} (see Fig. 1). The reference point is fixed at the middle of the minimum geometry of states $|1\rangle$ and $|3\rangle$ so that $\bar{q}_i = q_i - (d_{i,1}/2 + d_{i,2}/2)$ and assuming that the baths are not correlated, one gets

$$H^{(3)} = \begin{pmatrix} -\Delta_1 + (\lambda_1 + \lambda_2)/4 & H_{\mathrm{DA},1} & 0 \\ H_{\mathrm{DA},1} & (\lambda_1 + \lambda_2)/4 & H_{\mathrm{DA},2} \\ 0 & H_{\mathrm{DA},2} & \Delta_2 + (\lambda_1 + \lambda_2)/4 \end{pmatrix} + H_{\mathrm{B}} + S_1 B_1 + S_2 B_2 \quad (22)$$

with two system operators

$$S_1 = \frac{1}{2}\begin{pmatrix} 1 & 0 & 0 \\ 0 & -1 & 0 \\ 0 & 0 & -1 \end{pmatrix} \quad (23a)$$

$$S_2 = \frac{1}{2}\begin{pmatrix} 1 & 0 & 0 \\ 0 & 1 & 0 \\ 0 & 0 & -1 \end{pmatrix} \quad (23b)$$

Spectral density

The main tool of reduced equations describing the evolution of the electronic system is the autocorrelation function of the fluctuating force, in other words the autocorrelation function of the collective

coordinate B_j occurring in the system–bath coupling for each electronic transfer. The relevant time correlation function is then

$$C_j(t - t') = \mathrm{Tr}_\mathrm{B}[B_j(t)B_j(t')\rho_{\mathrm{B,eq}}] \quad (24)$$

where the trace is taken over the bath degrees of freedom. $\rho_{\mathrm{B,eq}}$ is the density matrix of a canonical ensemble of harmonic oscillators at the studied temperature and $B_j(t) = \mathrm{e}^{\mathrm{i}H_{\mathrm{B},j}t}B_j\mathrm{e}^{-\mathrm{i}H_{\mathrm{B},j}t}$ is the Heisenberg representation of the collective coordinate. The spectral density determining the system bath coupling at every frequency is defined as

$$J(\omega) = \frac{\pi}{2}\sum_{i=1}^{M}\frac{c_i^2}{\omega_i}\delta(\omega - \omega_i) \quad (25)$$

with $J(-\omega) = -J(\omega)$ (odd function). The relation between C_j and J is

$$C_j(t) = \frac{1}{\pi}\int_{-\infty}^{+\infty}\frac{J_j(\omega)\mathrm{e}^{\mathrm{i}\omega t}}{\mathrm{e}^{\beta\omega} - 1}\mathrm{d}\omega \quad (26)$$

The energy gap ΔE_j fluctuates due to the classical collective coordinates so that in the linear coupling case $C_j^{\mathrm{cl}}(t) = \langle\delta\Delta E_j(0)\delta\Delta E_j(t)\rangle = \langle B_j^{\mathrm{cl}}(0)B_j^{\mathrm{cl}}(t)\rangle$. An important step is then to relate the classical correlation function of the energy gap that can be obtained from (cDFT/MM) MD simulations, to the quantum counterparts or similarly to obtain $J_j(\omega)$ from $C_j^{\mathrm{cl}}(t)$. Various approaches can be found in the literature.[85–88] The classical and quantum functions have different symmetries. $C_j^{\mathrm{cl}}(t)$ is real and symmetric in time reversal operation $C_j^{\mathrm{cl}}(-t) = C_j^{\mathrm{cl}}(t)$ while the quantum correlation function is characterized by the relation assuring the detailed balance property $C_j(-t) = C_j(t)^\star = C_j(t - \mathrm{i}\beta\hbar)$ where $\beta = 1/k_\mathrm{B}T$. The Fourier transform (FT) of $C_j^{\mathrm{cl}}(t)$ reads

$$G_j^{\mathrm{cl}}(\omega) = \int_{-\infty}^{+\infty}C_j^{\mathrm{cl}}(t)\mathrm{e}^{\mathrm{i}\omega t}\mathrm{d}t = 2\int_0^{+\infty}C_j^{\mathrm{cl}}(t)\cos(\omega t)\mathrm{d}t \quad (27)$$

$G_j^{\mathrm{cl}}(\omega)$ is only a symmetrical real function while the FT of a quantum correlation function should give

$$G_j(\omega) = \int_{-\infty}^{+\infty}C_j(t)\mathrm{e}^{\mathrm{i}\omega t}\mathrm{d}t = G_{j,S}(\omega) + G_{j,A}(\omega) \quad (28)$$

The spectral density is in fact the antisymmetric part $J_j(\omega) = G_{j,A}(\omega)$. Different approaches have been proposed to obtain $G_{j,A}(\omega)$ from $G_j^{\mathrm{cl}}(\omega) = G_{j,S}(\omega)$. We adopt the so-called "harmonic correction" which leads to

$$J_j(\omega) = \frac{\beta\omega}{2}G_j^{\mathrm{cl}}(\omega) \quad (29)$$

The harmonic correction model satisfies the detailed balance relationship and postulates a harmonic bath. Other models are available in the literature[87] and selecting one particular model is a difficult task, since it can be system or temperature dependent. As already mentioned, the spectral density provides the other computation of the renormalization energy $\lambda_j = 1/2\sum_i \omega_i^2 d_{i,j}^2$ by eqn (8). Each ET step is characterized by its spectral density and we assume that the two baths are not correlated, in other words the cross correlation $C_{jk}(t) = \langle B_j(0)B_k(t)\rangle$ is neglected in a first approximation. This corresponds to the hypothesis that a deformation affecting a given ET has no influence on the other transfer.

Hierarchical equations of motion

The electronic system is represented by a two by two density matrix whose diagonal elements give the population in each electronic state and the off diagonal ones are the electronic coherences which are expected to decay by interaction with the vibrational bath. It is obtained by tracing out the bath modes from the full density matrix $\rho_\mathrm{S}(t) = \mathrm{Tr}_\mathrm{B}[\rho_{\mathrm{tot}}(t)]$. Initially the system and the environment are assumed to be decoupled. In other words the initial full density matrix is factorized $\rho_{\mathrm{tot}}(t) = \rho_\mathrm{S}(t)\rho_\mathrm{B}$ where ρ_B is the Boltzmann equilibrium density matrix. A vast array of literature reports has been devoted to the description of the reduced dynamics starting from the Vernon and Feynman influence functional of the projection methods according to Nakajima–Zwanzig or Shibata–Takabashi formalism.[89,90] The main issue is to go beyond any Markovian approximation when the correlation time of the bath remains of the same order of magnitude as the typical timescale of the system dynamics. The non-Markovian quantum master equation takes into account the full history of the system-environment exchange. Beyond non-Markovian approaches in the perturbative regime,[34–42,91,92] the HEOM method allows us to address strong system–bath coupling and converges towards the exact result. In practice, however, numerical limitations allow full convergence only for small system matrices and smooth spectral densities. To apply this algorithm, the spectral density is first decomposed into a sum of Lorentzian functions as already proposed for the perturbative[34] treatment.

$$J_j(\omega) = \sum_k^m p_{j,k}\frac{\omega}{\left[\left(\omega + \Omega_{j,k}\right)^2 + \Gamma_{j,k}^2\right]\left[\left(\omega - \Omega_{j,k}\right)^2 + \Gamma_{j,k}^2\right]} \quad (30)$$

By using eqn (26), the correlation function takes the form of an exponential series[93]

$$C_k(t) = \sum_k^K \alpha_{j,k}\mathrm{e}^{\mathrm{i}\gamma_{j,k}t} \quad (31)$$

where $2m$ terms stem from the poles of $J_j(\omega)$, namely $\alpha_{2l-1} = \frac{p_l}{8\Omega_l\Gamma_l}[\coth(\beta(\Omega_l \pm \mathrm{i}\Gamma_l)/2) \mp 1]$ and $\gamma_{2l-1} = \pm\Omega_l + \mathrm{i}\Gamma_l$ for $l = 1,\ldots m$ and $\alpha_k = 2\mathrm{i}J_0(\mathrm{i}\nu)$, $\gamma_k = \mathrm{i}\nu_k$ for $k > 2m$ where $\nu_k = 2\pi(k - 2m)/\beta$ are the Matsubara frequencies associated with the poles of the Bose function. The number of Matsubara terms is *a priori* infinite but can always be truncated in practice and the effective number decreases with increasing temperature.

The system reduced density matrix is then the first element of a chain of auxiliary density matrices $\rho_{\boldsymbol{n}}(t)$ where $\boldsymbol{n}$ is a global index of K non-negative integer numbers $\boldsymbol{n} = \{n_1,\ldots,n_k,\ldots,n_m\}$ with K the number of exponential terms in the expansion of the correlation function. The hierarchy is built with L levels. Each level is coupled to the next or the previous one. The level $L = 1$ corresponds to the system matrix $\rho_\mathrm{S} = \rho_0$ with the vector $\mathbf{0} = \{0,\ldots,0,\ldots,0\}$. For instance, when $K = 2$, there are two auxiliary

matrices with {1,0} and {0,1} at level $L = 2$ and three matrices {2,0}, {1,1} and {0,2} at level $L = 3$. The subscripts $\boldsymbol{n}_k^+$ and $\boldsymbol{n}_k^-$ denote $\{n_1,\ldots,n_{k+1},\ldots,n_m\}$ and $\{n_1,\ldots,n_{k-1},\ldots,n_m\}$ respectively, *i.e.* the subscript k denotes the rank of the index which is increased or decreased by one unity. The evolution is driven by time local coupled equations. For a single system operator S and by setting $\hbar = 1$, they read

$$\dot{\rho}_{\boldsymbol{n}}(t) = -\mathrm{i}[H_S, \rho_{\boldsymbol{n}}(t)] + \mathrm{i}\sum_k n_k\gamma_k\rho_{\boldsymbol{n}}(t) - \mathrm{i}\left[S, \sum_k \rho_{\boldsymbol{n}_k^+}(t)\right] - \mathrm{i}\sum_k n_k\left(\alpha_k S\rho_{\boldsymbol{n}_k^-} - \tilde{\alpha}_k\rho_{\boldsymbol{n}_k^-}S\right) \quad (32)$$

where $\tilde{\alpha}_{2l-1} = \alpha_{2l}{}^*$ and $\tilde{\alpha}_{2l} = \alpha_{2l-1}{}^*$ for $l = 1,\ldots,m$ and $\tilde{\alpha}_k = \alpha_k$ for $k > 2m$ For the three-state case, when the bath correlation is neglected, the baths act independently and it is possible to build two hierarchies related to each system operator S_1 and S_2 respectively with the parameters of each expansion of the correlation functions.

3. Results

We now turn to the presentation of our results. First we analyze the outcomes of the QM/MM MD simulations for ET steps 1 and 2 taken separately (see Fig. 1). The driving force and reorganization energies are discussed and analyzed through the different components of the molecular system. We then proceed to the calculation of the ET rates for the two steps. Non-Condon and nuclear tunneling contributions are assessed. We finally present the results of the quantum dissipative dynamics.

Kinetics models

Driving force and reorganization energy. Driving force ($-\Delta A^0$) and reorganization energy calculated according to eqn (4)–(6) are given in Table 1. Both ET steps ($W_{377} \rightarrow W_{400}{}^+$ and $W_{324} \rightarrow W_{377}{}^+$) are found to be exergonic for each initial configuration with average $\overline{\Delta A^0}$ values of −0.51 and −0.44 eV respectively. The Stokes reorganization energies are rather large, amounting to 1.17 and 1.68 eV on average. Values in the same range are obtained for λ^{var} and λ^J. We recall however that we have used here a non-polarizable force field, which commonly results in overestimations of redox reorganization energies by around 30%. Scaling down the lambdas by this percentage suggests more reasonable values around 0.8 and 1.2 eV respectively. We mention that λ^{St} and λ^{var} were not strongly sensitive to the length of the MD simulation from 5 to 30 ps (see ESI†). Reorganization energies obtained from the variance of the energy gap are found on average to be only slightly greater than Stokes reorganization energies, except for the second ET step in trajectories 1 and 3. This tends to show that although ETs within the tryptophan triad of *At*Cry take place on the picosecond time-scale, non-ergodicity effects in this system should be limited.[52] Concerning λ^{var} and λ^J, we find differences of a few hundredths of an eV or more in some cases, although the two quantities should be equal from a mathematical point of view. In fact our analysis showed that it is the finite durations of our cDFT/MD simulations that cause deviations between λ^{var} and λ^J. Increasing the time lag used to calculate the autocorrelation function of the diabatic energy gaps when calculating the spectral density function by eqn (9) helps reduce the discrepancy between the two quantities.

We now proceed to the analysis of the decomposition of ΔA^0 and λ into contributions from the inner- and outer-spheres. The values reported in Table 2 for the driving force show that, for both ET steps, almost all the stabilization of the product state essentially stems from the environment. The inner-sphere contributes weakly to ΔA^0 for the first ET step but is significant for the second step. Actually, the inner-sphere term encompasses two contributions: the intrinsic propensity of the tryptophan fragment (resp. the tryptophanyl radical) to be oxidized (resp. to be reduced) and the electrostatic interaction between the redox partners. To estimate the importance of the latter, we estimated its contribution to $\Delta A^0_{\mathrm{inner}}$ by applying a classical Coulomb law using the Hirshfeld charges calculated by cDFT on the tryptophan atoms along the MD simulations. The results are given in brackets in Table 2. The inter-tryptophan electrostatic

Table 1 Reorganization energies and free energy of the $W_{377} \rightarrow W_{400}{}^+$ (ET1) and $W_{324} \rightarrow W_{377}{}^+$ (ET2) ET steps. All energies are given in eV

	λ^{St}		$\lambda^{\mathrm{var}\,a}$		$\lambda^{J\,a}$		ΔA^0	
	ET1	ET2	ET1	ET2	ET1	ET2	ET1	ET2
1	1.14	1.89	1.07	2.19	1.07	1.75	−0.48	−0.29
2	1.17	1.80	1.37	1.80	1.32	1.54	−0.44	−0.51
3	1.14	1.74	1.12	2.83	1.06	2.01	−0.59	−0.11
4	1.17	1.49	1.33	1.37	1.28	1.39	−0.66	−0.82
5	1.21	1.50	1.42	1.54	1.31	1.63	−0.39	−0.47
Avg.	1.17	1.68	1.26	1.95	1.21	1.66	−0.51	−0.44

[a] Averages made over MD trajectories conducted on the initial and final diabatic states for the two ET steps, see Table S1 (ESI).

Table 2 Inner- *vs.* outer-sphere contributions of the effective free and reorganization energies. Energies are given in eV. Eqn (15) was used for evaluating the inner- and outer-sphere contributions to ΔE. The numbers in brackets are the contribution to $\Delta A^0_{\mathrm{inner}}$ from the electrostatic interaction between the pairs of tryptophan residues (see also main text)

	$\lambda^{\mathrm{St}}_{\mathrm{inner}}$	$\lambda^{\mathrm{St}}_{\mathrm{embed}}$	$\lambda^{\mathrm{var}}_{\mathrm{inner}}$	$\lambda^{\mathrm{var}}_{\mathrm{embed}}$	$\lambda^{\mathrm{var}}_{\mathrm{cross}}$	$\Delta A^0_{\mathrm{inner}}$	$\Delta A^0_{\mathrm{embed}}$
ET1							
1	0.26	0.88	0.24	0.91	0.02	−0.02 (0.04)	−0.46
2	0.27	0.91	0.29	1.12	<0.01	−0.01 (0.07)	−0.43
3	0.25	0.88	0.31	0.87	<0.01	−0.03 (−0.04)	−0.54
4	0.26	0.89	0.27	1.05	0.02	−0.03 (0.04)	−0.64
5	0.25	0.96	0.29	1.40	−0.01	−0.00 (0.06)	−0.39
Avg.	0.26	0.90	0.28	1.07	<0.01	−0.02 (0.03)	−0.50
ET2							
1	0.30	1.58	0.31	2.11	0.01	0.146 (0.129)	−0.44
2	0.29	1.51	0.25	1.68	−0.09	0.105 (0.089)	−0.61
3	0.31	1.43	0.34	3.15	0.10	0.155 (0.081)	−0.27
4	0.26	1.23	0.40	1.24	−0.06	0.064 (0.172)	−0.88
5	0.27	1.23	0.35	1.20	<−0.01	0.063 (0.113)	−0.53
Avg.	0.29	1.40	0.33	1.88	<−0.01	0.107 (0.117)	−0.55

interaction accounts well for the amplitude of $\Delta A^0_{\text{inner}}$. For the first ET step this contribution is, as $\Delta A^0_{\text{inner}}$, close to zero. For the second ET step it is almost equal to $\Delta A^0_{\text{inner}}$. The fact that the electrostatic interaction between the two redox partners is not the same for each ET step results from the different relative orientations of the tryptophan residues.

By difference, this result also means that the contribution to $\Delta A^0_{\text{inner}}$ from the ionization potential of the neutral tryptophan and from the electron affinity of the tryptophanyl radical is very small. This further indicates that there are only little differences in the polarization of the electron clouds between the two redox states, which eliminates the risk of non-linear effects due to high polarizability of the redox cofactors.[50] This conclusion is very likely to be relevant for other charge transfer chains in other proteins that involve tryptophan or tyrosine residues for instance.

The reorganization energy is also largely determined by the environment. The inner–outer cross reorganization energy term is extremely low (<0.01 eV in absolute value) for most trajectories, revealing a lack of correlation between the inner- and outer-spheres. This can be understood by considering that inner-sphere reorganization is due to bond length compression/lengthening upon ET, a process that is largely governed by local interactions (Coulomb repulsion and exchange interaction) at the space scales of covalent bonds inside the indole moieties. From a technical point of view this is an interesting result justifying the use of QM + MM approaches in which reorganization energies and driving forces are evaluated separately for the inner- and outer-spheres.[94] QM + MM schemes are appealing because the inner-sphere contributions can be obtained from a few quantum chemistry calculations on gas phase optimized geometries[94] in contrast to plain QM/MM calculations as reported in this article. The lack of strong correlation between the inner- and outer-sphere contributions ensures that such an approach is justified in the present case. It has in fact been followed recently to investigate charge separation in *Xl* (6-4) Pl.[17]

To go one step further in the analysis of the reorganization energy, we decompose the outer-sphere energy gap according to eqn (16) and (17) into contributions from the protein, the $FAD^{\bullet -}$ cofactor, the water molecules, the counter-ions and finally the ATP molecule (which docks to *At*Cry near the flavin).[18] To make this decomposition technically easier we recall that a classical approximation of the cDFT/MM energy gap has been made (see section the Simulation details). Primes are thus used to label the contributions to the outer-sphere reorganization energies calculated using eqn (17) and to distinguish them from those reported in Table 2 based on the true cDFT/MM energies. As expected the water ($\lambda'^{\text{var}}_{\text{WAT}}$) and protein ($\lambda'^{\text{var}}_{\text{prot}}$) contributions are the main contributions (Table 3 and Table S2, ESI†). The flavin ($\lambda'^{\text{var}}_{\text{FAD}}$), adenosine triphosphate ($\lambda'^{\text{var}}_{\text{ATP}}$) and counterion ($\lambda'^{\text{var}}_{\text{ions}}$) contributions are small, representing on average 5, 2 and 2.6% of $\lambda'^{\text{var}}_{\text{total}}$ respectively. The cross correlation ($\lambda'^{\text{var}}_{\text{cross}}$) contribution is on the contrary rather large, showing that there exists a strong correlation among certain components. It turns out that only the protein–water cross reorganization energy is important, with the other cross terms being negligible. It is certainly attributable to water molecules localized at the protein surface, in particular, close to the tryptophan triad. Fig. 2 depicts the cumulative Stokes reorganization energy due to water molecules as a function of the distance between the center of mass of each tryptophan pairs. Solvent reorganization is found to be much larger for the second ET step due to the larger exposure of the tryptophan pair to the solvent. This interpretation is corroborated by the radial distribution functions shown in Fig. 2.

Table 3 Average contributions to the outer-sphere reorganization energy calculated using eqn (17). The data are computed from simulations performed on state CT1 (respectively CT2) for ET1 (respectively ET2). All energies are given in eV

	$\lambda'^{\text{var}}_{\text{FAD}}$	$\lambda'^{\text{var}}_{\text{WAT}}$	$\lambda'^{\text{var}}_{\text{prot}}$	$\lambda'^{\text{var}}_{\text{ATP}}$	$\lambda'^{\text{var}}_{\text{ions}}$	$\lambda'^{\text{var}}_{\text{cross}}$
ET1	0.08	0.76	0.76	0.03	0.04	−0.56
ET2	0.02	2.37	0.86	0.03	0.05	−1.57

Fluctuations of energy gaps and electronic coupling

Electronic coupling amounts to a few tens of meV (Table 4). These values are close to those reported for *Xl* (6-4) photolyase,[17] obtained also from cDFT calculations. In contrast they are approximately ten times larger than values reported previously in *At*Cry.[20] In ref. 20 the authors used a Fragment-Based Tight-Binding DFT methodology. For the first ET step we observed very few sign changes of H_{DA} in the course of the simulations,

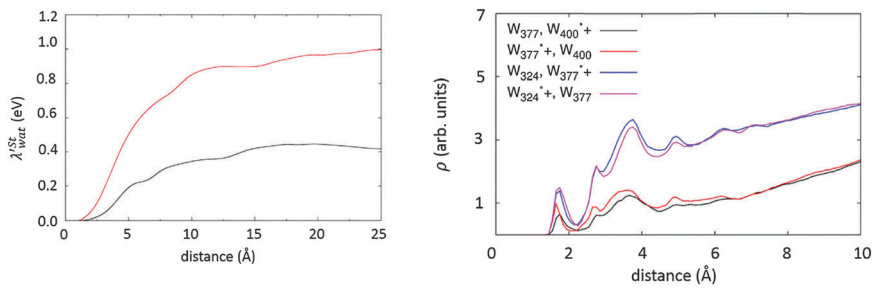

Fig. 2 Left: Cumulative Stokes reorganization energy of water molecules as a function of distance from the center of mass of the tryptophan pair for each ET step (ET1 in black, ET2 in red). Right: Radial distribution function of oxygen atoms as a function of the distance from the center of mass of the tryptophan pair for each ET step. The curves are averaged over the five sets of MD simulations for each step.

Table 4 Interplay between electronic coupling and energy gap fluctuations. $\langle H_{DA}\rangle$ and $\langle H_{DA}^2\rangle$ are given in meV and (meV)^2 respectively, the characteristic times τ_{coh} and τ_{FC} in fs

	$\langle H_{DA}\rangle$	$\langle H_{DA}^2\rangle$	R_{coh}	τ_{coh}	τ_{FC}
ET1					
1	6.88	94.4	0.50	26	22
2	26.3	776.63	0.89	35	39
3	15.9	385.25	0.66	95	32
4	4.33	78.27	0.24	38	42
5	19.9	598.13	0.67	73	58
Avg.	14.7	386.54	0.59	54	39
ET2					
1	25.9	796.94	0.85	34	78
2	−1.53	520.12	0.01	35	40
3	25.6	801.18	0.82	12	141
4	35.5	2010.05	0.63	61	35
5	−33.2	2389.33	0.46	37	17
Avg.	10.5	1303.53	0.55	36	62

suggesting that the same kinds of ET pathways are activated throughout the simulations, consistently with the fact that the two involved tryptophan residues preserve their respective orientations during the simulations. The coherence parameter defined as $R_{coh} = \langle H_{DA}\rangle^2/\langle H_{DA}^2\rangle$[54] falls in the range [0.25, 0.90] for most trajectories, which is consistent with a tunneling process governed by the average structure (Table 4).[95] A noticeable exception is the second trajectory for the second ET step for which a coherence parameter of only 0.01 is found. This is a consequence of multiple sign changes of the electronic coupling which results from the relative orientation of the two tryptophans. The upper panel of Fig. 3 shows the normalized auto-correlation functions of H_{DA}. They all decay with characteristic times (τ_{coh}) of a few tens of femtoseconds, taking τ_{coh} as the time taken for the coupling to decay to 1/e. The values of τ_{coh} obtained here on the order of few tens of femtoseconds are reminiscent of the time scales reported for other proteins such as modified azurins,[55] C-clamp[96] molecules or in the PRC.[97]

The lower panels of Fig. 3 depict the ACF of the vertical energy gap for the cDFT/MM MD simulations. The curves decay to zero within a few hundreds of femtoseconds. A Franck–Condon time (τ_{FC}) is defined as the time taken by the ACF of the energy gap to drop to 1/e. However the tails of the ACF do not reach zero after 4 ps, meaning that residual correlations persist at these time scales. We note on the other hand that all curves rapidly drop to 1/e within less than 50 fs (see inset graphs). On short time scales both ΔE and H_{DA} fluctuate at a similar speed. Values of similar order were reported recently by Mallus *et al.* using semi-empirical quantum chemistry methodologies.[98] If the electronic coupling fluctuates much faster than the vertical energy gap, the non-Condon approximation underlying eqn (1) may breakdown.[53,55,95] To test this eventuality we have computed the ET rates with the formalism proposed by Troisi *et al.* and given by eqn (10)–(12).[24, 96] For the sake of comparison with results obtained in the following sections we have used λ^J (*in lieu* of λ^{var}) values in our calculations of ET rates. As seen from the numbers reported in Table 5, non-Condon effects are negligible for the first step, being less than 3% on average. This result is in line with the rather large value of R_{coh}. Results for the second transfer are more contrasted. For trajectories 1, 4 and 5, non-Condon corrections are again very small for the same reasons (large R_{coh} and τ_{coh} values). For trajectories 2 and 3, non-Condon corrections are significant as a result of the small R_{coh} values (0.01) or small τ_{coh} (12 fs) respectively.

Assessment of nuclear tunneling on ET rates

We now investigate the influence of nuclear tunneling on ET rates. Table 5 gathers ET rates calculated using the mixed-quantum classical expression given by eqn (13). With this

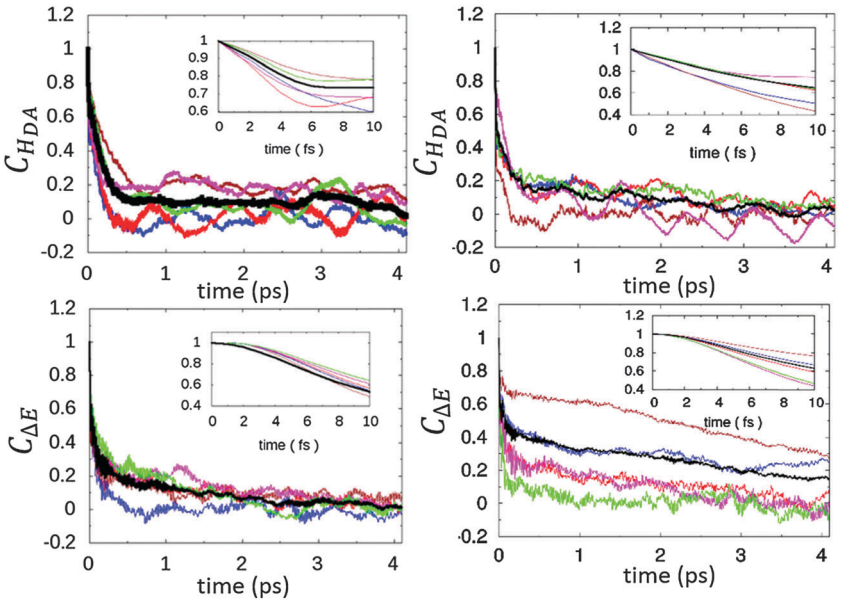

Fig. 3 Top: Normalized ACF of the electronic coupling. Bottom: Normalized ACF of the vertical energy gap. The left panel refers to ET step 1 while the right panel refers to ET step 2. Each color curve corresponds to one cDFT/MM MD trajectory. The black curve is the average curve. Inset: Zoom on the first 10 fs.

Table 5 ET rates calculated. The number in brackets are $k^{(2)}/k^{(0)}$. Rates are given in 10^{10} s^{-1}. ω_{qc} is given in cm^{-1}

	Eqn (10)–(12)		Eqn (13)		Eqn (33)
	$k^{(0)}$	$k^{(2)}$	ω_{qc} = 500	ω_{qc} = 4000	QM + MM
ET1					
1	5.21	0.38 (0.073)	69.26	5.21	14.12
2	3.90	0.06 (0.016)	101.64	3.90	162.07
3	83.4	0.16 (0.002)	473.48	83.4	335.11
4	6.20	0.25 (0.041)	46.51	6.20	67.35
5	1.73	0.02 (0.012)	42.70	1.73	27.90
Avg.	20.1	0.17 (0.029)	146.72	20.1	121.31
ET2					
1	0.02	0.0007 (0.04)	4.93	0.02	3.31
2	2.94	0.41 (0.14)	79.56	2.94	16.11
3	0.00003	0.00002 (0.73)	0.014	0.00003	23.12
4	160.86	1.29 (0.008)	1842.17	160.86	275.76
5	1.00	0.10 (0.10)	839.75	1.00	96.54
Avg.	32.96	0.36 (0.20)	553.28	32.96	82.97

formalism ω_{qc} is a cutting frequency between vibrational modes treated at the quantum or at the classical level. For ω_{qc} set to 4000 cm^{-1} we expect to recover the rates given by eqn (3) which is the classical limit of Marcus theory. This is actually the case. For ω_{qc} set to 500 cm^{-1} the ET rate is increased by factors 8 and 17 for ET steps 1 and 2 compared to the classical treatment, attesting the significance of nuclear tunneling in ET in these proteins. On average steps 1 and 2 take place on the sub-picosecond time scale when nuclear tunneling is taken into account. However the computed rates are scattered with the initial conditions and some rates are found on the picosecond time scale. To identify if nuclear tunneling mainly involves inner-sphere motions (the tryptophan residues) or if some environment mode also contribute, we have proceeded to another quantum-classical partition which is not based on the cutting frequency ω_{qc} but on the cDFT/MM energy partition.

$$k = \frac{2\pi}{\hbar}\langle H_{DA}{}^2\rangle \frac{1}{\sqrt{4\pi\lambda_o^J k_B T}} \times \exp\left(\frac{-(\Delta A^0 + \lambda_o^{St})^2}{4\lambda_o^J k_B T} - \frac{1}{\pi\hbar}\int_0^\infty \frac{J_{inner}(\omega)}{\omega^2} d\omega\right) \quad (33)$$

In eqn (33) λ_o^J is the outer-sphere reorganization energy calculated by eqn (8) with the outer-sphere spectral density $J_{outer}(\omega)$. The latter was itself computed by eqn (9) using the outer-sphere energy gap (ΔE_{embed} see eqn (15)). λ_o^{St} is obtained similarly using eqn (5). Inner-sphere contributions are treated at the quantum mechanical level, introducing the inner-sphere spectral density J_{inner} obtained from the autocorrelation function of ΔE_{inner} (eqn (15)).

It is found that inner-sphere modes introduce pronounced nuclear quantum effects, a conclusion which is reminiscent to our study of the *Xl* (6-4) photolyase for which a Jortner–Bixon formalism was used.[17] However the data provided in Table 5 also indicate that the outer-sphere significantly contributes to nuclear tunneling effects on ET rates. As can be seen in Fig. 4 the spectral density for both ET steps exhibits numerous peaks

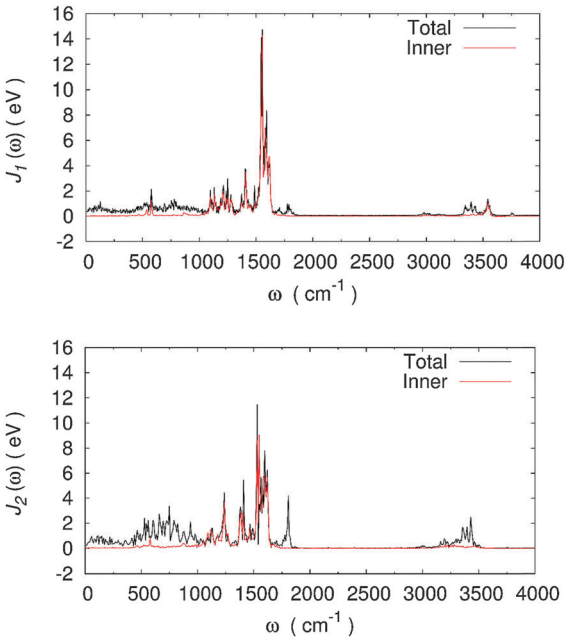

Fig. 4 Spectral density obtained from the average of the auto-correlation functions of the energy gaps over five cDFT/MM MD simulations for each ET step. The red line is calculated from the inner-sphere energy terms only (J_{inner}).

arising from the inner-sphere (red curves). Nonetheless it is seen by difference with the black curves, which represents the spectral density obtained with the full cDFT/MM energy gaps, that the protein and solvent molecules have coupled modes in the [500–3500] cm^{-1} range. This is especially true for ET2 where the peaks between 3000 and 3500 cm^{-1} in the spectral density are due to the outer sphere. The presence of such contributions for ET2 is not surprising because of the larger solvent exposure of the tryptophan pair involved (see Fig. 2) solvation difference (this frequency range is typically the one of O–H bond vibrations).

In Fig. 5 we present the evolution of the populations over the entire tryptophan triad resulting from the application of a classical two-successive-step kinetic model. We neglected back-reactions because of the high free-energies of activation that are associated with back electron transfers. The three panels correspond to the data reported in Table 5 (Avg. lines). With the fully classical Marcus rate expressions hole transfer to the third tryptophan of the triad is expected within a few ps. The inclusion of nuclear quantum effects either by shifting the cutting frequency to 500 cm^{-1} (eqn (13)) or by treating only the inner-sphere contribution quantum-mechanically significantly reduces the time for the overall process. We emphasize however that kinetics data presented in Table 5 or in Fig. 5 apparently indicate rates that are too fast compared to the available experimental data on this family of proteins.[9] In fact the computational estimates are extremely sensitive to small variations in the parameters entering the rate expressions. This is true for the electronic coupling or for the reorganization energies for example. As a consequence the rates may be under- or over-estimated by

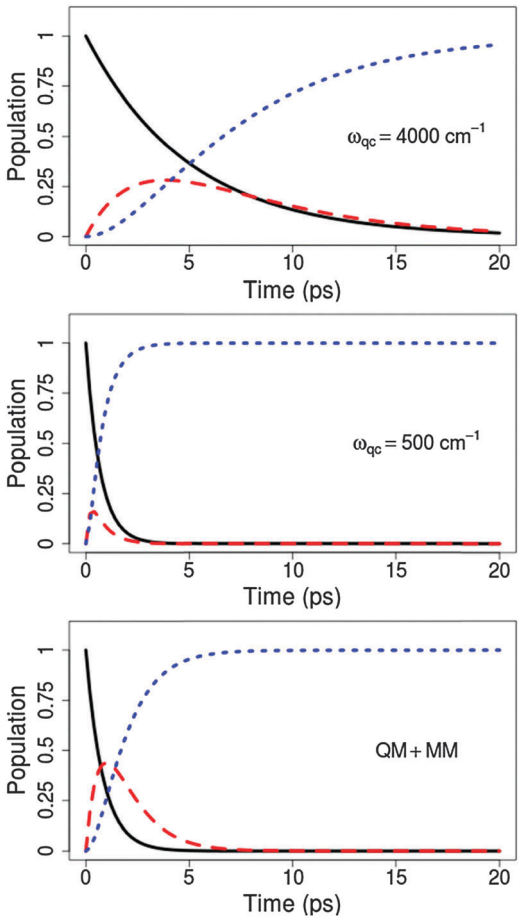

Fig. 5 Evolution of the populations of the three diabatic states involved in electron transfers assuming a two-successive-steps kinetic model (identifying concentrations as populations). The kinetic equations were solved with the data of Table 5 assuming that only the initial state is initially populated. The black, red and blue curves correspond to the first, second and third diabatic state respectively. Top and middle: eqn (13) has been used with two values of the cutting frequencies. Bottom eqn (33) has been used.

a few orders of magnitude. What is probably more relevant for the present discussion are the trends observed when comparing the two ET steps or when assessing the influence of quantum effects.

Dissipative quantum dynamics

To get insight into the quantum electron transfer we examine the spin-boson model by averaging the five classical correlation functions obtained from the QM/MM trajectories. The electronic Hamiltonian H_s is calibrated also by the average of the square of the electronic coupling and an average bias (see the Methodology section). The dissipative model is treated in the framework of the HEOM method. This approach enables us to treat strongly coupled non-Markovian systems but it may become very expensive when the spectral density is very structured leading to a lot of terms in the expansion of the correlation function. We began by checking the stability of approximate results obtained by smoothing the spectral density of ET1 by five Lorentzian functions according to eqn (30). They are shown in the upper-left panel of Fig. 6. However, the strong non-Markovian behavior of this system requires rising to a high level of the hierarchy (40th order for the first transfer and 80th order for the second one). As we expect the low frequency deformations of the protein to play a significant role, we always keep two Lorentzians to cover the low-frequency region and we eventually add a third one centered on higher frequency regions. We did not add any Matsubara terms that correspond to the high temperature limit. The lower-left panel of Fig. 6 shows the evolution of the population in the first diabatic state during ET1. At least two Lorentzians covering the 0–1000 cm^{-1} region are needed to stabilize the evolution of the population. The inclusion of a third Lorentzian centered around 1200, 1600 or 3500 cm^{-1} does not significantly modify the overall decay of the diabatic populations. The main result of this quantum simulation is to emphasize the role of the environment which is characterized by rather low frequencies, in the electron transfer process. The results of a similar study for the second ET step are presented in the right panels of Fig. 6. Again at least two Lorentzians fitting the low frequency range up to 1000 cm^{-1} are necessary to reach stable results regarding the evolution of the diabatic populations. However, when including a third Lorentzian DQD turns out to be numerically unreachable (9 366 819 auxiliary matrices must be used) at the 80th order due to local implementation limitations. We thus proceed with the calculation up to the 40th order only leading to numerical instabilities: only the initial decrease of population is stable here. The strong system–bath coupling and the highly structured spectral density make this application particularly difficult. Several implementations might overcome this issue with massively parallel filtering algorithms[40,99] or GPU implementation.[45]

The relative stability of the calculations validates the approximation with two Lorentzians and suggests that the three-state case can be treated by retaining only two Lorentzians for both spectral densities. Panel a of Fig. 7 displays the populations for the three-state case. The evolution is in nice agreement with the classical kinetic scheme discussed previously based on the results of eqn (13) and (33) and shown in Fig. 5. The initial state is depopulated in about 1 ps. The full transfer *via* ET1 and ET2 requires about 4 ps. Now, contrary to the kinetic treatment followed in the previous section, the quantum approach described here gives insights into coherences (see panels c and d). We first recall that in the diabatic representation, only the imaginary parts are relevant to measure the decrease of coherence. The timescale for complete coherence loss is about 1 ps. The real part can go to a non-vanishing value corresponding to the weight of the diabatic states in the adiabatic ground state. Panel b displays the purity of the $Tr[\rho_S^2]$ system. One observes the decrease of the purity and the slow evolution towards a statistical mixture. We are here in a particular case for which the mixture contains only the ground electronic state due to the Boltzmann weights and therefore $Tr[\rho_S^2]$ becomes again equal to one. So the expected final statistical mixture is again a pure state here.

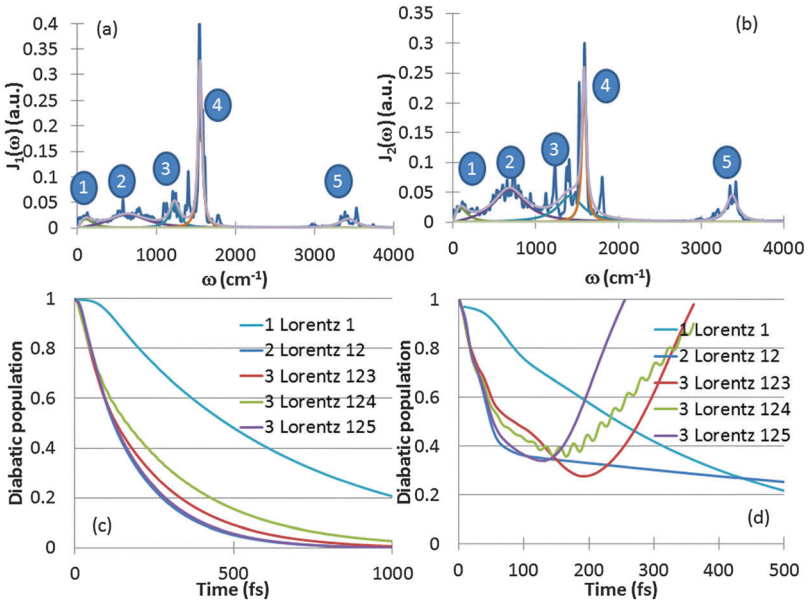

Fig. 6 Top: Fitting of the average spectral density functions obtained from cDFT/MM MD simulations (see Fig. 4) by five Lorentzian functions. Panel a refers to the first ET step and panel b to the second ET step. Bottom: Evolution of the diabatic populations in the course of the DQD propagation for different sets of Lorentzian functions picked in the ensemble of the 5 functions depicted on the graphs of the upper panels.

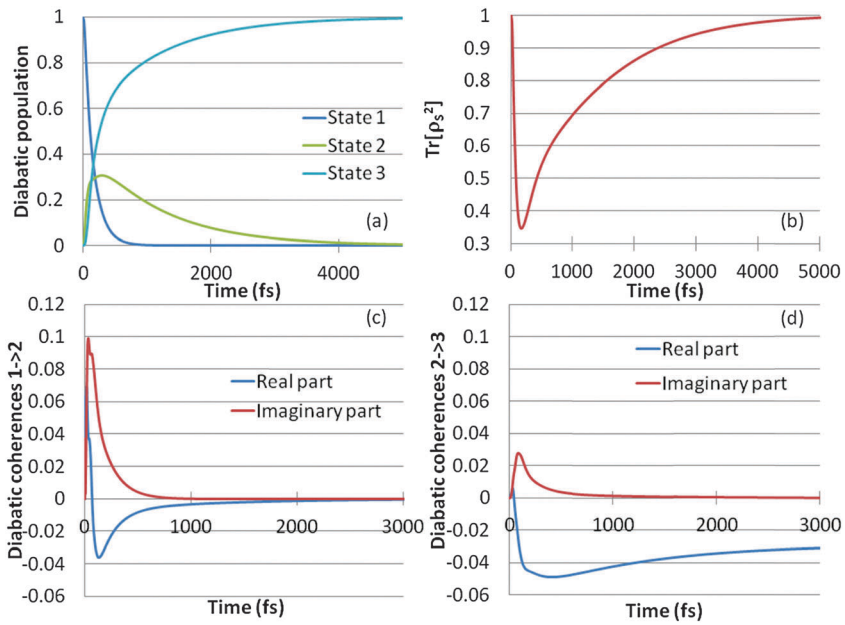

Fig. 7 Results of the DQD for the three state model. Panel a: evolution of the population in the three diabatic states, pane b: purity of the system measured by Tr[ρ_S^2]; bottom: coherences between the diabatic states for the first ET step (panel c) and the second ET step (panel d).

4. Conclusion

In this article we have been interested in ultrafast charge separation in *Arabidopsis thaliana* cryptochrome, and more particularly in quantum effects associated with electron transfers between the tryptophan residues. We have devised a dedicated computational strategy based on the realization of *ab initio* QM/MM MD simulations using constrained DFT as the quantum method to define the diabatic potential energy surfaces of interest, and to estimate the electronic coupling between the relevant electronic states. This approach allowed us to reach a level of description that had not been reached by previous simulations of electron transfer in Cry or Pl. The thermodynamics parameters governing the inter-tryptophan electron transfers have been decomposed in terms of contribution from the redox fragments, the protein residues and the

water molecules. Our methodology enabled us to assess various effects such as non-Condon effect and nuclear tunneling in these proteins. A current limitation of our present QM/MM approach, however, is the absence of electronic polarization of the environment, but efforts in that direction are currently underway in our laboratories. The second important achievement of this work is to have implemented an HEOM algorithm to deal with ET in proteins using the outputs of cDFT/MM MD simulations. The system of present interest leads to a particularly strong coupling between the electronic system and the low frequency deformations of the protein so that a non-perturbative treatment is required. The interplay of three electronic states with large electronic gaps and highly structured spectral densities renders this system computationally very challenging. The application of the HEOM method to charge separation in *At*Cry shed new light on the intimate quantum effects associated with these processes. Quantum effects are important to take into account to understand charge separation in *At*Cry. This conclusion is likely to be relevant for other proteins of the Cry and Pl superfamily. Another lesson learned is the applicability of the QM + MM approach. We also found that the occurrence of non-Condon effects strongly depends on the relative orientations of the tryptophan residues. They were shown to be negligible in most simulations of *At*Cry. However they may be more important in other proteins of the family if successive tryptophan or tyrosine residues are aligned in T-shape geometries, because in this case H_{DA} will frequently change sign and amount to zero on average. The calibrated models obtained in this work should enable future theoretical investigations of temperature dependence effects on the ET rate in cryptochromes and photolyases.

More generally we think the dual approach followed in this work, combining on one hand state-of-the-art QM/MM simulations coupled to cDFT to define realistic model Hamiltonians, and on the other hand, advanced algorithms for quantum dynamics should benefit several other ET processes taking place in biomolecules like proteins or DNA but also non-biological systems.

Acknowledgements

We are grateful to Compute Canada/WestGrid for generous computational resources. This work was performed using HPC resources from GENCI [CCRT/CINES/IDRIS] (Grant 2014-2015, project number x2015076913). This work was supported by the ANR programs *Investissements d'Avenir du LabEx PALM* (Grant ANR-10-LABX-0039-PALM). We acknowledge support from the CoConicS Project (ANR-13-BS08-0013-03). This work has been performed within the French network GDR 3575 THEMS.

References

1 C. Aubert, M. H. Vos, P. Mathis, A. P. M. Eker and K. Brettel, *Nature*, 2000, **405**, 586–590.
2 I. Chaves, R. Pokorny, M. Byrdin, N. Hoang, T. Ritz, K. Brettel, L.-O. Essen, G. T. J. van der Horst, A. Batschauer and M. Ahmad, *Annu. Rev. Plant Biol.*, 2011, **62**, 335–364.
3 N. W. Woodbury, M. Becker, D. Middendorf and W. W. Parson, *Biochemistry*, 1985, **24**, 7516–7521.
4 A. M. Nuijs, H. Vasmel, H. L. P. Joppe, L. N. M. Duysens and J. Amesz, *Biochim. Biophys. Acta, Bioenerg.*, 1985, **807**, 24–34.
5 J. Deisenhofer and J. R. Norris, *Photosynthetic Reaction Center*, Elsevier Science, 2013.
6 A. Sancar, *Chem. Rev.*, 2003, **103**, 2203–2238.
7 H. Park, S. Kim, A. Sancar and J. Deisenhofer, *Science*, 1995, **268**, 1866–1872.
8 R. Brudler, K. Hitomi, H. Daiyasu, H. Toh, K.-i. Kucho, M. Ishiura, M. Kanehisa, V. A. Roberts, T. Todo, J. A. Tainer and E. D. Getzoff, *Mol. Cell*, 2003, **11**, 59–67.
9 D. Immeln, A. Weigel, T. Kottke and J. L. Pérez Lustres, *J. Am. Chem. Soc.*, 2012, **134**, 12536–12546.
10 Y.-T. Kao, C. Saxena, T.-F. He, L. Guo, L. Wang, A. Sancar and D. Zhong, *J. Am. Chem. Soc.*, 2008, **130**, 13132–13139.
11 J. Shirdel, P. Zirak, A. Penzkofer, H. Breitkreuz and E. Wolf, *Chem. Phys.*, 2008, **352**, 35–47.
12 J. Brazard, A. Usman, F. Lacombat, C. Ley, M. M. Martin, P. Plaza, L. Mony, M. Heijde, G. Zabulon and C. Bowler, *J. Am. Chem. Soc.*, 2010, **132**, 4935–4945.
13 A. Lukacs, A. P. M. Eker, M. Byrdin, K. Brettel and M. H. Vos, *J. Am. Chem. Soc.*, 2008, **130**, 14394–14395.
14 P. Müller, J. Yamamoto, R. Martin, S. Iwai and K. Brettel, *Chem. Commun.*, 2015, **51**, 15502–15505.
15 D. V. Matyushov, *J. Phys.: Condens. Matter*, 2015, **27**, 473001.
16 P. B. Woiczikowski, T. Steinbrecher, T. Kubař and M. Elstner, *J. Phys. Chem. B*, 2011, **115**, 9846–9863.
17 F. Cailliez, P. Müller, T. Firmino, P. Pernot and A. de la Lande, *J. Am. Chem. Soc.*, 2016, **138**, 1904–1915.
18 F. Cailliez, P. Müller, M. Gallois and A. de la Lande, *J. Am. Chem. Soc.*, 2014, **136**, 12974–12986.
19 W. Humphrey, A. Dalke and K. Schulten, *J. Mol. Graphics*, 1996, **14**, 33–38.
20 G. Lüdemann, I. A. Solov'yov, T. Kubař and M. Elstner, *J. Am. Chem. Soc.*, 2015, **137**, 1147–1156.
21 P. H. Dederichs, S. Blügel, R. Zeller and H. Akai, *Phys. Rev. Lett.*, 1984, **53**, 2512–2515.
22 Q. Wu and T. Van Voorhis, *Phys. Rev. A: At., Mol., Opt. Phys.*, 2005, **72**, 024502.
23 T. V. Voorhis, T. Kowalczyk, B. Kaduk, L.-P. Wang, C.-L. Cheng and Q. Wu, *Annu. Rev. Phys. Chem.*, 2010, **61**, 149–170.
24 A. Troisi, A. Nitzan and M. A. Ratner, *J. Chem. Phys.*, 2003, **119**, 5782–5788.
25 X. Song and A. A. Stuchebrukhov, *J. Chem. Phys.*, 1993, **99**, 969–978.
26 V. May and O. Kühn, *Charge and Energy Transfer Dynamics in Molecular Systems*, Wiley-VCH Verlag GmbH & Co. KGaA, 3rd edn, 2011.
27 U. Weiss, in *Quantum Dissipative Systems*, ed. I. E. Dzyaloshinskii, S. O. Lundqvist and Y. Lu, Singapore, 2012, vol. 10.
28 H. D. Meyer, U. Manthe and L. S. Cederbaum, *Chem. Phys. Lett.*, 1990, **165**, 73–78.
29 H. Wang and M. Thoss, *J. Chem. Phys.*, 2003, **119**, 1289–1299.
30 U. Manthe, *J. Chem. Phys.*, 2008, **128**, 164116.

31 J. Schulze and O. Kühn, *J. Phys. Chem. B*, 2015, **119**, 6211–6216.
32 O. Vendrell and H.-D. Meyer, *J. Chem. Phys.*, 2011, **134**, 044135.
33 E. Mangaud, A. de la Lande, C. Meier and M. Desouter-Lecomte, *Phys. Chem. Chem. Phys.*, 2015, **17**, 30889–30903.
34 C. Meier and D. J. Tannor, *J. Chem. Phys.*, 1999, **111**, 3365–3376.
35 A. Ishizaki and Y. Tanimura, *J. Phys. Soc. Jpn.*, 2005, **74**, 3131–3134.
36 Y. Tanimura, *J. Phys. Soc. Jpn.*, 2006, **75**, 082001.
37 Y. Tanimura and R. Kubo, *J. Phys. Soc. Jpn.*, 1989, **58**, 101–114.
38 M. Tanaka and Y. Tanimura, *J. Chem. Phys.*, 2010, **132**, 214502.
39 A. Ishizaki and G. R. Fleming, *J. Chem. Phys.*, 2009, **130**, 234111.
40 J. Strümpfer and K. Schulten, *J. Chem. Theory Comput.*, 2012, **8**, 2808–2816.
41 H. Liu, L. Zhu, S. Bai and Q. Shi, *J. Chem. Phys.*, 2014, **140**, 134106.
42 J. Zhu, S. Kais, P. Rebentrost and A. Aspuru-Guzik, *J. Phys. Chem. B*, 2011, **115**, 1531–1537.
43 K. H. Hughes, B. Cahier, R. Martinazzo, H. Tamura and I. Burghardt, *Chem. Phys.*, 2014, **442**, 111–118.
44 A. Ishizaki and G. R. Fleming, *Proc. Natl. Acad. Sci. U. S. A.*, 2009, **106**, 17255–17260.
45 C. Kreisbeck, T. Kramer, M. Rodríguez and B. Hein, *J. Chem. Theory Comput.*, 2011, **7**, 2166–2174.
46 R. R. Dogonadze, M. K. Alexander and A. A. Chernenko, *Russ. Chem. Rev.*, 1965, **34**, 759.
47 R. A. Marcus and N. Sutin, *Biochim. Biophys. Acta*, 1985, **811**, 265–322.
48 A. Warshel, *J. Phys. Chem.*, 1982, **86**, 2218–2224.
49 G. King and A. Warshel, *J. Chem. Phys.*, 1990, **93**, 8682–8692.
50 D. N. LeBard, V. Kapko and D. V. Matyushov, *J. Phys. Chem. B*, 2008, **112**, 10322–10342.
51 D. N. LeBard and D. V. Matyushov, *J. Phys. Chem. B*, 2009, **113**, 12424–12437.
52 D. V. Matyushov, *J. Chem. Phys.*, 2013, **139**, 025102.
53 E. S. Medvedev and A. A. Stuchebrukhov, *J. Chem. Phys.*, 1997, **107**, 3821–3831.
54 I. A. Balabin and J. N. Onuchic, *Science*, 2000, **290**, 114–117.
55 S. S. Skourtis, I. A. Balabin, T. Kawatsu and D. N. Beratan, *Proc. Natl. Acad. Sci. U. S. A.*, 2005, **102**, 3552–3557.
56 S. Efrima and M. Bixon, *Chem. Phys.*, 1976, **13**, 447–460.
57 J. Jortner and M. Bixon, *J. Chem. Phys.*, 1988, **88**, 167–170.
58 J. K. Hwang and A. Warshel, *Chem. Phys. Lett.*, 1997, **271**, 223–225.
59 F. Cailliez, P. Müller, T. Firmino, P. Pernot and A. de la Lande, *J. Am. Chem. Soc.*, 2016, **138**, 1904–1915.
60 A. M. Koster, P. Calaminici, M. E. Casida, V. D. Dominguez, R. Flores-Moreno, G. Geudtner, A. Goursot, T. Heine, A. Ipatov, F. Janetzko, J. M. del Campo, J. U. Reveles, A. Vela, B. Zuniga and D. R. Salahub, *deMon2k*, The deMon developers, Mexico City, 2nd edn, 2011.
61 A. de la Lande and D. R. Salahub, *THEOCHEM*, 2010, **943**, 115–120.
62 J. Řezáč, B. Lévy, I. Demachy and A. de la Lande, *J. Chem. Theory Comput.*, 2012, **8**, 418–427.
63 A. Warshel and M. Levitt, *J. Mol. Biol.*, 1976, **103**, 227–249.
64 B. R. Brooks, C. L. Brooks III, A. D. Mackerell Jr, L. Nilsson, R. J. Petrella, B. Roux, Y. Won, G. Archontis, C. Bartels, S. Boresch, A. Caflisch, L. Caves, Q. Cui, A. R. Dinner, M. Feig, S. Fischer, J. Gao, M. Hodoscek, W. Im, K. Kuczera, T. Lazaridis, J. Ma, V. Ovchinnikov, E. Paci, R. W. Pastor, C. B. Post, J. Z. Pu, M. Schaefer, B. Tidor, R. M. Venable, H. L. Woodcock, X. Wu, W. Yang, D. M. York and M. Karplus, *J. Comput. Chem.*, 2009, **30**, 1545–1614.
65 A. D. Mackerell, M. Feig and C. L. Brooks, *J. Comput. Chem.*, 2004, **25**, 1400–1415.
66 A. D. MacKerell, D. Bashford, M. Bellott, R. L. Dunbrack, J. D. Evanseck, M. J. Field, S. Fischer, J. Gao, H. Guo, S. Ha, D. Joseph-McCarthy, L. Kuchnir, K. Kuczera, F. T. K. Lau, C. Mattos, S. Michnick, T. Ngo, D. T. Nguyen, B. Prodhom, W. E. Reiher, B. Roux, M. Schlenkrich, J. C. Smith, R. Stote, J. Straub, M. Watanabe, J. Wiórkiewicz-Kuczera, D. Yin and M. Karplus, *J. Phys. Chem. B*, 1998, **102**, 3586–3616.
67 J. P. Perdew, K. Burke and M. Ernzerhof, *Phys. Rev. Lett.*, 1996, **77**, 3865–3868.
68 P. Calaminici, F. Janetzko, A. M. Köster, R. Mejia-Olvera and B. Zuniga-Gutierrez, *J. Chem. Phys.*, 2007, **126**, 044108.
69 J. W. Mintmire and B. I. Dunlap, *Phys. Rev. A: At., Mol., Opt. Phys.*, 1982, **25**, 88–95.
70 A. M. Köster, J. U. Reveles and J. M. del Campo, *J. Chem. Phys.*, 2004, **121**, 3417–3424.
71 P. Calaminici, R. Flores-Moreno and A. Köster, *Comput. Lett.*, 2005, **1**, 164–171.
72 Q. Wu and T. Van Voorhis, *J. Chem. Theory Comput.*, 2006, **2**, 765–774.
73 F. L. Hirshfeld, *Theor. Chim. Acta*, 1977, **44**, 129–138.
74 J. Řezáč, *J. Comput. Chem.*, 2016, **37**, 1230–1237.
75 S. Dapprich, I. Komáromi, K. S. Byun, K. Morokuma and M. J. Frisch, *THEOCHEM*, 1999, **461–462**, 1–21.
76 A. Alvarez-Ibarra, A. M. Köster, R. Zhang and D. R. Salahub, *J. Chem. Theory Comput.*, 2012, **8**, 4232–4238.
77 W. L. Jorgensen, J. Chandrasekhar, J. D. Madura, R. W. Impey and M. L. Klein, *J. Chem. Phys.*, 1983, **79**, 926–935.
78 S. Nosé, *Mol. Phys.*, 1984, **52**, 255–268.
79 W. G. Hoover, *Phys. Rev. A: At., Mol., Opt. Phys.*, 1985, **31**, 1695–1697.
80 Q. Wu and T. Van Voorhis, *J. Chem. Phys.*, 2006, **125**, 164105.
81 A. Kubas, F. Hoffmann, A. Heck, H. Oberhofer, M. Elstner and J. Blumberger, *J. Chem. Phys.*, 2014, **140**, 104105.
82 A. Kubas, F. Gajdos, A. Heck, H. Oberhofer, M. Elstner and J. Blumberger, *Phys. Chem. Chem. Phys.*, 2015, **17**, 14342–14354.
83 D. Mejía-Rodríguez and A. M. Köster, *J. Chem. Phys.*, 2014, **141**, 124114.
84 A. J. Leggett, S. Chakravarty, A. T. Dorsey, M. P. A. Fisher, A. Garg and W. Zwerger, *Rev. Mod. Phys.*, 1987, **59**, 1–85.

85 S. A. Egorov, K. F. Everitt and J. L. Skinner, *J. Phys. Chem. A*, 1999, **103**, 9494–9499.
86 S. Shim, P. Rebentrost, S. Valleau and A. Aspuru-Guzik, *Biophys. J.*, 2012, **102**, 649–660.
87 S. Valleau, A. Eisfeld and A. Aspuru-Guzik, *J. Chem. Phys.*, 2012, **137**, 224103.
88 C. Olbrich, J. Strümpfer, K. Schulten and U. Kleinekathöfer, *J. Phys. Chem. Lett.*, 2011, **2**, 1771–1776.
89 R. Zwanzig, *J. Chem. Phys.*, 1960, **33**, 1338–1341.
90 F. Shibata, Y. Takahashi and N. Hashitsume, *J. Stat. Phys.*, 1977, **17**, 171–187.
91 S.-H. Yeh, J. Zhu and S. Kais, *J. Chem. Phys.*, 2012, **137**, 084110.
92 U. Kleinekathöfer, *J. Chem. Phys.*, 2004, **121**, 2505–2514.
93 A. Pomyalov, C. Meier and D. J. Tannor, *Chem. Phys.*, 2010, **370**, 98–108.
94 J. Blumberger, *Phys. Chem. Chem. Phys.*, 2008, **10**, 5651–5667.
95 D. N. Beratan, C. Liu, A. Migliore, N. F. Polizzi, S. S. Skourtis, P. Zhang and Y. Zhang, *Acc. Chem. Res.*, 2015, **48**, 474–481.
96 A. Troisi, M. A. Ratner and M. B. Zimmt, *J. Am. Chem. Soc.*, 2004, **126**, 2215–2224.
97 H. Nishioka, A. Kimura, T. Yamato, T. Kawatsu and T. Kakitani, *J. Phys. Chem. B*, 2005, **109**, 15621–15635.
98 M. I. Mallus, M. Aghtar, S. Chandrasekaran, G. Lüdemann, M. Elstner and U. Kleinekathöfer, *J. Phys. Chem. Lett.*, 2016, 1102–1108.
99 Q. Shi, L. Chen, G. Nan, R.-X. Xu and Y. Yan, *J. Chem. Phys.*, 2009, **130**, 084105.